# Chapter 3 Multibeam-waist modes

Lasers with various geometrically stable resonators usually support definite transverse modes, such as Hermite-Gaussian mode or Laguerre-Gaussian mode. However, a specific resonator configuration with its round trip transfer matrix $M = \begin{bmatrix} A & B \\ C & D \end{bmatrix}$ that satisfies M^n equal to the identity matrix, where n is an integer, does not prefer a specific mode but is capable of supporting arbitrary transverse modes. For these resonator configurations the gain effect may dominate the transverse mode distribution. As a matter of fact, it has been demonstrated that the transverse mode can self-adjust its pattern to fit the pumped volume in the self-imaging confocal cavity [1]. Besides, because of gain-guiding, some unusual transverse modes were observed in an end-pumped $Nd:YVO_4$ laser [2,3]. Recently, using a sufficiently tightly focused pump, Wu. et al. observed unusual modes [4,5] in an end-pumped $Nd:YVO_4$ laser with a plano-concave cavity near degeneracy of $g_1g_2 = 1/4$ (i.e., 1/3 transverse frequency degeneracy) as well as $g_1g_2 = 1/2$ (1/4-degeneracy). This mode for $g_1g_2 = 1/4$ has a near-field pattern with a small waist on the flat mirror end; nevertheless, it has a far-field pattern with many concentric rings [5]. In particular, this mode exhibits three beam waists when it is propagated through a transform lens [4]. In this chapter, we numerically simulate the feature of the multibeam-waist (MBW) mode by using a mode-calculation procedure, and the results not only show good agreement with previous experiments but also lead to more experimental observations. In addition, we explain why the modes exhibit such behaviors and give them a mathematical representation.

The numerical model has been described in Section 2.1 except that we fixed R and ρ throughout this chapter. Because we concern mainly about the transverse

mode distribution, we do not consider the dispersion of the active medium and the frequency detuning between the atomic transition and the cavity mode, thus the gain is assumed to be real. The thermal effect is also neglected. Furthermore, we magnify the value of γ by 100 times to obtain the continuous-wave solution because transverse mode distribution is independent of γ as long as Δt (the round trip time) $\ll 1/\gamma$. Given an initial ΔN and E, after the power output undergoing a procedure similar to the relaxation oscillation, the field distribution E converges to a cw steady-state solution. Such a numerically convergent solution is equivalent to a theoretical one-round-trip self-consistent solution. In our simulation, the aperture was chosen 1-mm that is much larger than the empty cavity beam radius of 108 μm for $g_1 g_2 = 1/4$. To implement Collin integral by the Romberg method, we divided 1-mm aperture radius into 2048 segments.
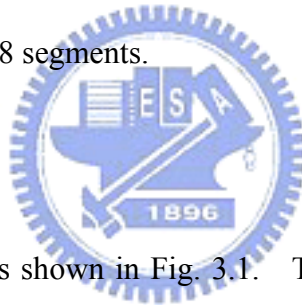
3.1 Experimental set up

The experimental setup is shown in Fig. 3.1. This laser contains a 1mm-thick Nd:YVO$_4$ crystal and an output coupler with R = 8 cm having 10% transmission at the lasing wavelength of 1.064 μm. The face of the crystal that faced the pump beam had a dichroic coating with greater than 99.8% reflection at 1.064 μm and greater than 99.5 % transmission at the pump wavelength of 808 nm; the other surface comprised an antireflection layer at 1.064 μm to avoid the effects of intracavity etalons. The output coupler (OC) was mounted on a translation stage so we can tune the cavity length about the degenerate configurations. The pump beam source was a Ti-sapphire laser operated in cw output with a nearly TEM$_{00}$ mode. A collimating lens (CL) was added in front of the crystal such that we could tune the pump size, and the lens was simultaneously used to transform the near-field mode pattern on the crystal to the screen. The laser output was split into two beams, one

of which was used to project the far-field pattern onto the screen or was sent to a rf spectrum analyzer via a photodetector (PD); the other was propagated through a transform lens and then was detected with a charge-coupled device (CCD). To directly image the mode pattern behind the transform lens and reduce the noise, we replaced the camera lens of the CCD by a laser line filter (LF). The near-Gaussian pump size is determined by the standard knife methods. The degeneration point is determined by the position where the lowest lasing threshold occurs [4,5].

3.2 Transverse mode pattern

We focused the simulations primarily on the configuration near 1/3-degeneracy to compare it with the experimental data. The parameters that we used are $\rho = 0.95$, $d = 1$ mm, $R = 8$ cm, $\lambda = 1.064$ μm, $1/\gamma = 50$ μs, $\sigma = 25 \times 10^{-19}$ cm^2, $N_0 = 1.7 \times 10^{20}$ cm^{-3}, and $E_s^2 = 1.12 \times 10^{10}$ joule/Farad-m^2. Choosing $w_p = 30$ μm and $P_p = 50$ mW, in Fig. 3.2(a) we show the numerical intensity distributions of the output fields on the flat mirror end, the near field for $L = 6$ cm (at degeneracy) and $L = 6.15$ cm (far from degeneracy), and the corresponding experimental mode patterns. Their far-field intensity profiles are shown in Fig. 3.2(b). To illustrate clearly the far-field ring structure for the case of degeneracy, we elevated its zero-intensity baseline in Fig. 3.2(b). We can see that the numerical results are in agreement with the experiments. The numerical near-field profiles in Fig. 3.2(a) show a small spot size of 27 μm at degeneracy, whereas a spot size of 87 μm far from degeneracy for a $1/e^2$ spot size is defined. The spot size shrinks to approximately the pump size when the cavity is tuned toward degeneracy; this means that the gain-guiding effect dominates the transverse mode pattern near degeneracy. From Figs. 3.2(a) and 3.2(b) the transverse mode near degeneracy exhibits several rings with low intensity on the axis in the far field but does not have a ring in the near field with peak intensity on the axis.

This reveals that the mode differs significantly from a usual mode and that its pattern depends on the propagation distance.

The numerical data also show the number of rings in the far field increases with decreasing pump size. However, far from degeneracy the near-field spot size in Fig. 3.2(a) approaches the cold-cavity beam waist size, and its far-field profile in Fig. 3.2(b) has a near-Gaussian distribution. This indicates that the transverse mode is a normal one and that the diffraction effect is more important than the gain effect in pattern formation far from degeneracy. Indeed, we suggest using small-size pumping to obtain the fundamental-mode operation with a low lasing threshold in end-pumped four-level solid-state lasers [6]. Moreover, if we vertically block the cavity beam with a knife in the near-degenerate cavity, parts of the far-field rings still survive, rather than completely disappear, as shown in Fig. 3.2(c). It must be noted that because of a lack of transverse mode beating, the transverse profiles described above are immune from detection in different parts of the profile; the use of the InGaAs fast detector with 200 ps response time and 60 dB dynamic range shows that these profiles are time-independent.

3.3 Beam propagation

We discuss the beam propagation shown in Fig. 3.3. Propagating the field solution of the case at degeneracy in Fig. 3.2(a) toward the output coupler (z = 6 cm) in the +z direction, we showed the beam-profile variation with propagation distance z [Fig. 3.3(a)]. Note that the numerical reference plane is on the flat mirror (z = 0 cm), where the well-known beam waist is located. We see a peculiar feature: the beam does not diverge but self-converges to form a waist close to the output coupler. In addition, the profile variation along z is unlike that of a beam whose profile maintains the same pattern, except that it increases its spot size with propagation distance. We

can add a transform lens (Fig. 3.1, TL) after the output coupler to monitor the beam-profile variation that reveals the z-dependence of the stationary mode and concurrently uncovers the main character of the three beam waists as follows.

If we place a transform lens with a focal length of 5.2 cm a distance of 10.5 cm from the output coupler as in the experiment [4], this is equivalent to propagating the field solution a distance of 16.5 cm and then through the transform lens.   Here we neglect the refraction from the finite thickness of the output coupler.   The variation of beam profile with propagation distance Z' is shown in Fig. 3.3(b), where Z' = 0 is the position of the transform lens.   We found there are three beam waists, at positions of Z' = 6.8, 7.6, 10.0 cm that match quite well the experimental observation [4], as is also shown in Fig 3.3(b).   Moreover, the intracavity beam profiles in Fig. 3.3(a) are transmitted to the respective positions from Z' = 7.6 to Z' = 10.3 cm that follow the Gaussian lens law.   For instance, the intracavity profiles at z = 1.0 and z = 3.0 cm have the same patterns as those of at Z' = 7.82 and Z' = 8.46 cm, respectively, where the observed profiles have low intensity on axis, as shown in Fig. 3.3(b).   The additional waist close to the output coupler in Fig. 3.3(a) is transformed on the plane Z' = 10.0 cm.

3.4 Ray geometry

By ray tracing we show the three beam-waist locations, at Z'_A, Z'_D, and Z'_{DI} , that are the images of the three objects A, D, and D_I, respectively, as illustrated in Fig. 3.4(a), where a paraxial ray from point A via B to F and back to A forms a closed ray path after three round trips in the cavity.   So it is reasonable to suppose that the peculiar beam may be a superposition of three sources, which are located at z = -L, 0, +L on the optical axis.

We found from the stability analysis of a conservative map involving only

Gaussian beam propagation in the plano-concave empty cavity that the resonator configuration with $g_1g_2 = 1/4$ has a period-3 orbit of a q-parameter [7]. We plot in Fig. 3.4(b) the q-parameter's evolution in the (w, 1/R) space with reference plane z_0 at the flat mirror (z = 0 cm) for the 1/3-degenerate empty cavity, where w is the spot size and 1/R is the curvature of the wave front. We can see the three states 1-3 of consecutive round trips form a set of period-3 solutions and that 1/R is the mismatch of the mirror curvature in states 2 and 3 if we assume that the wave front of state 1 matches the flat mirror. We use $E_{gi}(w_i, R_i; z_0)$, i = 1, 2, 3 to label a set of period-3 solutions (three successive round-trip electric fields of Gaussian distribution at the flat mirror) in Fig. 3.4(b) and sometimes abbreviate it as $E_{gi}(z_0)$ if w and R need not be emphasized. Any positive w_1 will follow a periodic evolution, which means there are infinite sets of period-3 solutions for an empty cavity of 1/3-degeneracy.

In accordance with Fig. 3.4(b), in Fig. 3.4(c) we depict the Gaussian-beam evolutionin in which the first round-trip wave begins with $E_{g1}(w_1 = aa'/2, R_1 = \infty; z_0)$ and reproduces itself after three round trips in the cold cavity. Note that a positive R represents a divergent wave riding in the propagation direction. The second round trip begins when $E_{g2}(w_2 = cc'/2, R_2; z_0)$ converges at dd'. The third round trip, with $E_{g3}(w_3 = w_2, R_3 = -R_2; z_0)$, is divergent from cc'; however, it seems to emanate from d_Id_I'. Thus the beam sources with waist sizes at aa', dd', and d_Id_I' correspond to $E_{gi}(z_0)$, i = 1, 2, 3, respectively. Moreover, in comparison with that in Fig. 3.4(a) and 3-4(c), the Gaussian-beam evolution from aa' to bb' is similar to rays AB and AF; then bb' and cc' act as the rays BC and FE, and so on. Point sources A, D, and D_I are therefore equivalent to the three beam sources at aa', dd', and d_Id_I', respectively. So far we have learn that three waists come from three point sources that act as three beam sources that correspond to $E_{gi}(z_0)$, i = 1, 2, and 3.

3.5 Period-3 superposition representation

We know from both experimental observation and mode calculation that the stationary cw laser output of 1/3-degeneracy is a one-round-trip self-consistent mode. It exhibits the ray-like character of three beam waists. The stationary cw laser field on any plane within the cavity is the accumulated electric fields of the successive round-trips. So we suspect that the electric field of the multibeam-waist mode of 1/3-degeneracy can be represented as the superposition of three consecutive fields of period-3 solution for the 1/3-degenerate empty cavity.

Because the gain medium lies against the flat mirror, we choose $w_1 = 27$ μm, the waist size of the intensity profile in Fig. 3.2(a), and propagate E_{g1} ($w_1 = 27$ μm, $R_1 = \infty$; z_0) in the empty cavity of $L = 6$ cm by using integral formula (2.1), which is equivalent to choosing a set of period-3 fields according to the gain effect. Then we obtain E_{g2} (z_0) and E_{g3} (z_0) after one and two round trips, respectively. Since the Guoy phase shift was not included in Eq. (2.1), we added a phase shift of π when the beam passed through the waists of aa' and dd' in Fig. 3.4(c). The period-3 superposed intensity profile $\left| E_{g1}(z_0) + E_{g2}(z_0) - E_{g3}(z_0) \right|^2$ is shown in Fig. 3.5 by open circles on a logarithmic vertical scale; also shown, by filled circles is the one-round-trip self-consistent mode normalized with respect to the superposed peak intensity. We see that the two profiles match well, except for small differences near the edge of the 1-mm aperture and near the intensity minimum at $r = 200$ μm. These deviations are discussed in Section 3.6 below. From such a representation, the observed behaviors can easily be understood. The small waist in the near-field pattern is due mainly to $\left| E_{g1}(z_0) \right|^2$ because it is much larger than $\left| E_{g2}(z_0) \right|^2$ and $\left| E_{g3}(z_0) \right|^2$. The self-convergent phenomenon in Fig. 3-3(a) results from the negative curvature of $E_{g2}(z_0)$ that converges there. The additional transformed waists at $Z' =$

48

6.8 cm and Z' = 10.0 cm in Fig. 3.3(b) are due mainly to the individual contribution of E_{g3} (z_0) and E_{g2} (z_0), respectively.   Because the propagation behaviors of $E_{g1}(z_0)$ + $E_{g2}(z_0)$ - $E_{g3}(z_0)$ are very similar to those shown in Fig. 3.3(a) and 3.3(b), the far-field ring pattern or any profiles on the transverse planes of z are the result of interference of the three Gaussian fields at z that emanates from E_{gi} (w_i,R_i;z_0), i = 1, 2, 3, respectively.   Therefore we conclude that the multibeam-waist mode distribution at z can be written as a period-3 superposition, namely $\Sigma^3_{i=1}$ E_{gi} ($w_i(z)$, $R_i(z)$; z).   The value of the period-N superposition representation is that it uncovers the main character of the MBW mode and substantially simplifies the mode representation.

For g_1g_2 = 1/2 the results of period-2 superposed field $E_{g1}(z_0)$ + $E_{g2}(z_0)$ match those of mode calculation and of experiments that show two waists behind a proper transform lens.   The spot size evolution is a period-2 orbit and the geometric picture is shown in Fig. 3.6.   Similarly, $E_{g1}(z_0)$ + $E_{g2}(z_0)$ + $E_{g3}(z_0)$ also simulates g_1g_2 = 3/4 well.   In particular, one can detect an additional waist outside the cavity without adding a transform lens, as shown in Fig 3.7.

3.6 Discussion and parameter dependence

The multibeam-waist modes discussed so far exhibit the duality of wave and ray optics, similarly geometric modes [2], in which the gain guide induces a preferred W-shaped closed ray path such that the light spots appear at the ray trace in an off-axis end-pumped Nd:YVO$_4$ laser near g_1g_2 = 1/2.   Ramsay and Degnan [8] have shown that the vertices of closed ray paths can be identified with the points of maximum field intensity in a CO$_2$ laser, so a closed ray path might be regarded as a mode.   However, our experimental observations indicate points B, C, E, and F of Fig. 3.4(a) are not local intensity maxima.   Therefore, the relationship between Fig. 3.4(a) and 3.4(c) is different from those shown in Refs. [2] and [8].   Furthermore, the ratio

of the pump size to the fundamental mode waist size is not an important factor for obtaining the geometric modes described in Ref. 2, for which a size ratio larger than 1 was used. Also because of the large pump region near degeneracy, the CO_2 laser described in Ref. [8] was operated in multitransverse modes, so there are mode patterns that correspond well to closed ray paths. However, small pump size is necessary and is an important parameter for achieving MBW modes.

The deviation between the two profiles in Fig. 3.5 near the aperture edge comes from the high-order Laguerre-Gaussian mode because we can add a small Laguerre-Gaussian component of high-order to E_{g1} to eliminate the small difference. Note that now E_{g1} is no longer a lowest-order Gaussian; however the mode still preserves the character of periodic superposition to exhibit three beam waists. That the high-order component is due to high pumping power is known from the fact that E_{g1} consists only of the lowest-order Gaussian as P_p decreased to 12 mW. Indeed, we observed three beam waists for pump powers from a little above the lasing threshold (7 mW) to 400 mW in the experiments. Even for high pump power, the higher-order Laguerre-Gaussian plays only a minor role and never changes the basic character of period-3 superposition. It must be mentioned that the multibeam-waist mode is independent of the longitudinal mode beating because it was detected for a large pump power range. Furthermore, increasing the pump power will increase w_1 of $E_{g1}(z_0)$ as a result of gain saturation, from ~20 to ~32 μm, corresponding to P_p from 12 to 200 mW for $w_p = 30$ μm. So the chosen w_1 discussed in Section 3.4 and 3.5 depends on the pumping power. Another difference, near r = 200 μm comes from a gain guide that changes configuration parameter g_1g_2. We can eliminate this deviation by superposing E_{g1}, E_{g2} and E_{g3} in the cavity of L = 6 + δ cm by replacing L = 6 cm, where δ is a small quantity. This confirms the influence of gain guiding.

Finally, we discuss the pump size and the cavity-length dependence. Figure

3.8 shows that the numerical lasing threshold varies with the pump size for $L = 6$ cm and 6.15 cm. The degenerate case has lower lasing threshold, and in fact we use it to determine the degeneration point in the experiments. For instance, the lasing threshold at degeneracy as $w_p = 30$ μm is ~8 mW, which matches the experiment well. It was also found that the threshold difference increases with decreasing w_p, so it is easier to excite the multibeam-waist mode with smaller w_p near degeneracy. As $w_p > 80$ μm the gain guide is too weak to excite the multibeam-waist mode. When the cavity was tuned away from degeneracy with w_p fixed, the waist position at Z'_D (see Fig. 3.4(a)) shifted and this waist gradually became indistinct. Finally, the three-beam-waist configuration is broken up far from degeneracy. The tuning range for achieving a multibeam-waist mode depends on w_p. Our numerical data show a full tuning range of ~700 μm for $w_p = 30$ μm. However, it is not easy to identify the exact tuning range as well as the pump size limit in experiments by observation of additional waists. The far-field ring structure together with the average power output therefore may become a good identifier.

References

[1] V. Couderc, O. Guy, A. Barthelemy, C. Froehly, and F. Louradour, Opt. Lett. 19, 1134 (1994).

[2] J. Dingjan, M.P. van Exter, J.P. Woerdman, Opt. Commun. 188, 345 (2001).

[3] N.J. van Druten, S.S.R. Oemrawsingh, Y. Lien, C. Serrat, M.P. van Exter, and J.P. Woerdman, J. Opt. Soc. Am. B 18, 1793 (2001).

[4] H.H. Wu and W.F. Hsieh, J. Opt. Soc. Am. B 18, 7 (2001).

[5] H.H. Wu, C.C. Sheu, T.W. Chen, M.D. Wei, and W.F. Hsieh, Opt. Commun. 165, 225 (1999).

[6] P. Laporta and M. Brussard, IEEE J. Quantum Electron. 27, 2319 (1991).

[7] M.D. Wei, W.F. Hsieh, C. C. Sung, Opt. Commun. 146, 201 (1998).

[8] I.A. Ramsay and J.J. Degnan, Appl. Opt. 9, 385-398 (1970).

[9] G.O. Harding and T. Li, J. Appl. Phys. 35, 475 (1964).

[10] T. Kimura, K. Otsuka, and M. Saruwatari, IEEE J. Quantum Electron. 7, 225 (1971).

[11] E. Louvergneaux, G. Slekys, D. Dangoisse, and P. Glorieux, Phy. Rev. A 57, 4899 (1998).
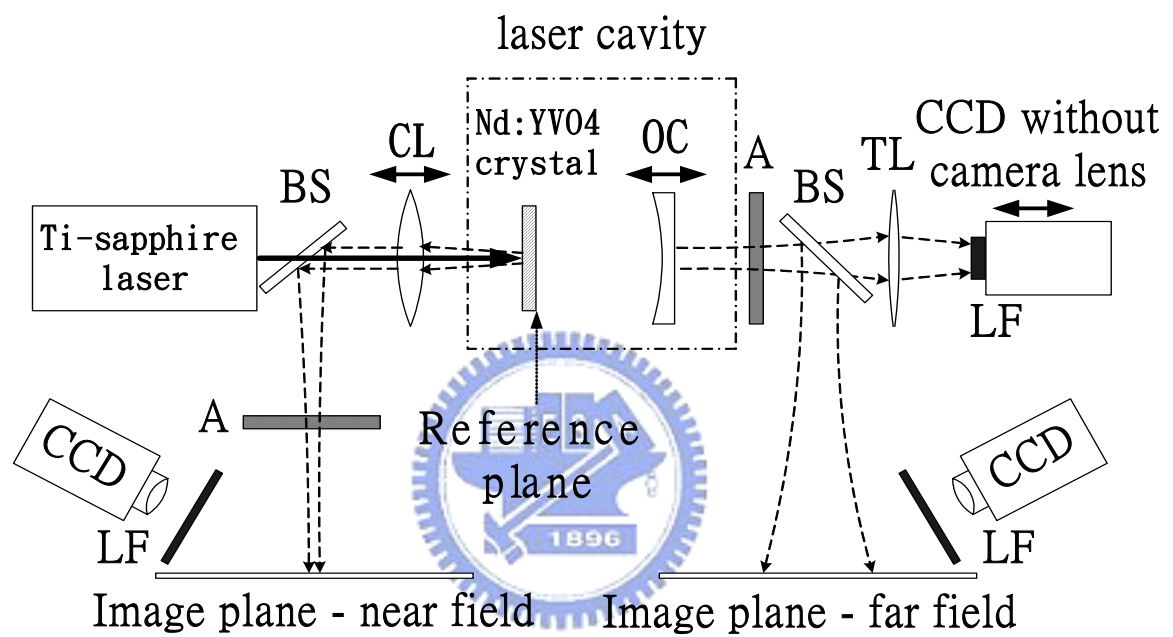
Fig. 3.1.   Schematic diagram of the experimental setup.   BS is a beam splitter, A is

an attenuator, and the others are in the text.
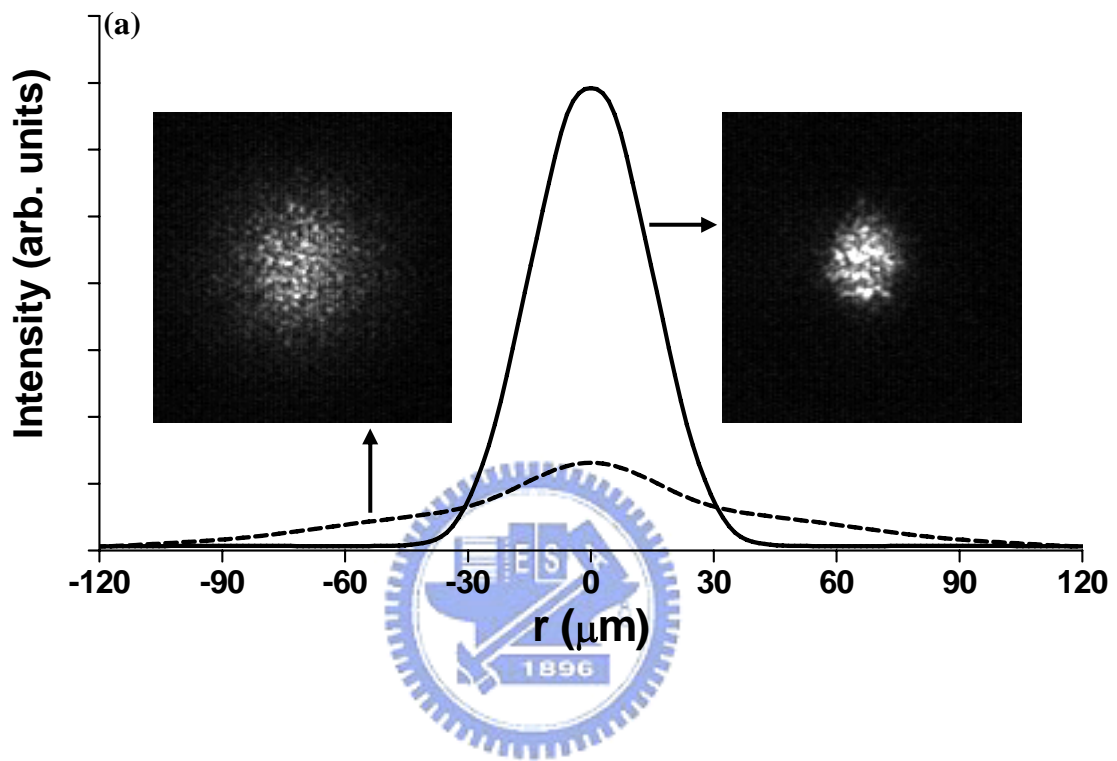
Fig. 3.2. (a) The numerical intensity profiles on the flat mirror end for L = 6 cm (solid line) and L = 6.15 cm (dash line) together with the corresponding experimental photographs of beam-waist patterns in the near field. The grains in photographs are due to reflection of the screen.
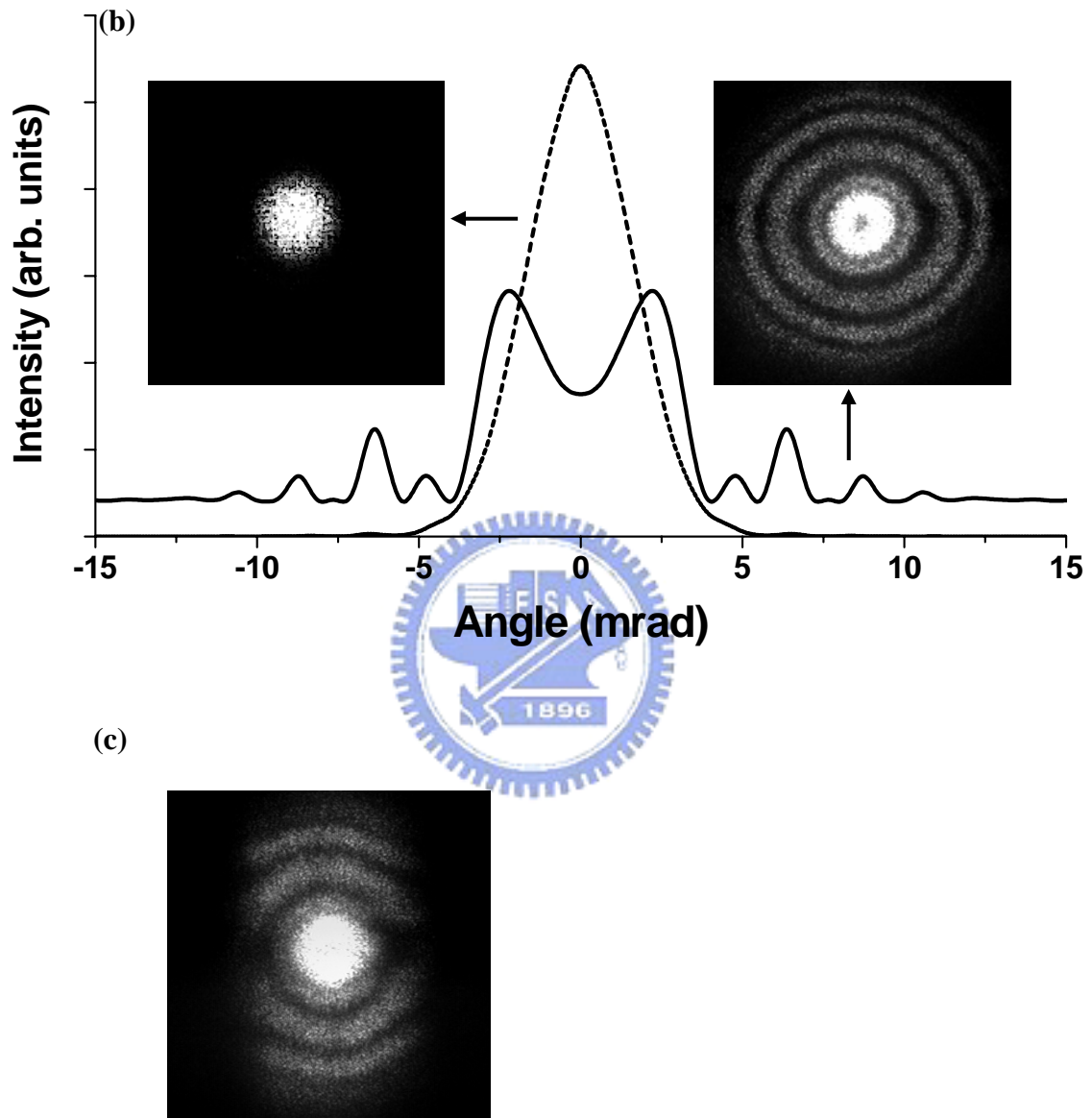
Fig. 3.2.   (b) The far-field intensity profiles corresponding to (a).   Solid line is for

degeneracy.   (c) Experimental far-field mode pattern as a knife set in the cavity.
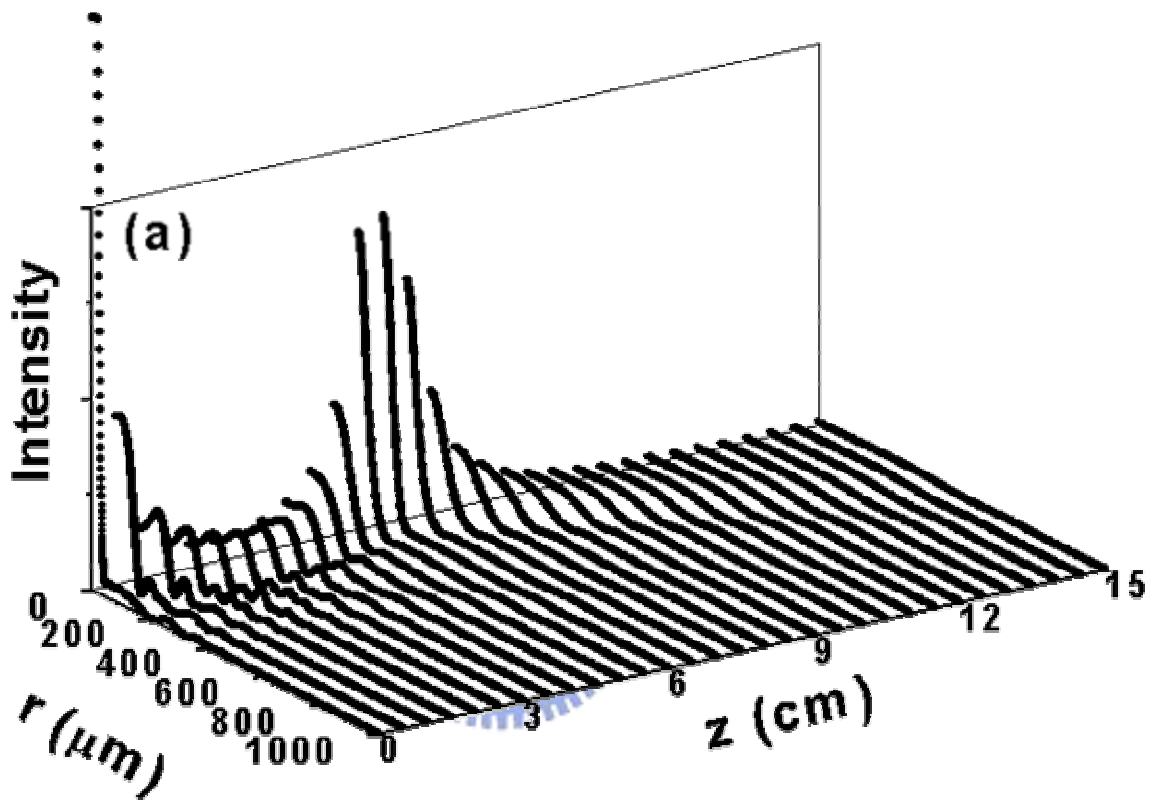
Fig. 3.3. (a) Propagating behavior for L = 6 cm in Fig. 3-2(a) through intracavity

space.
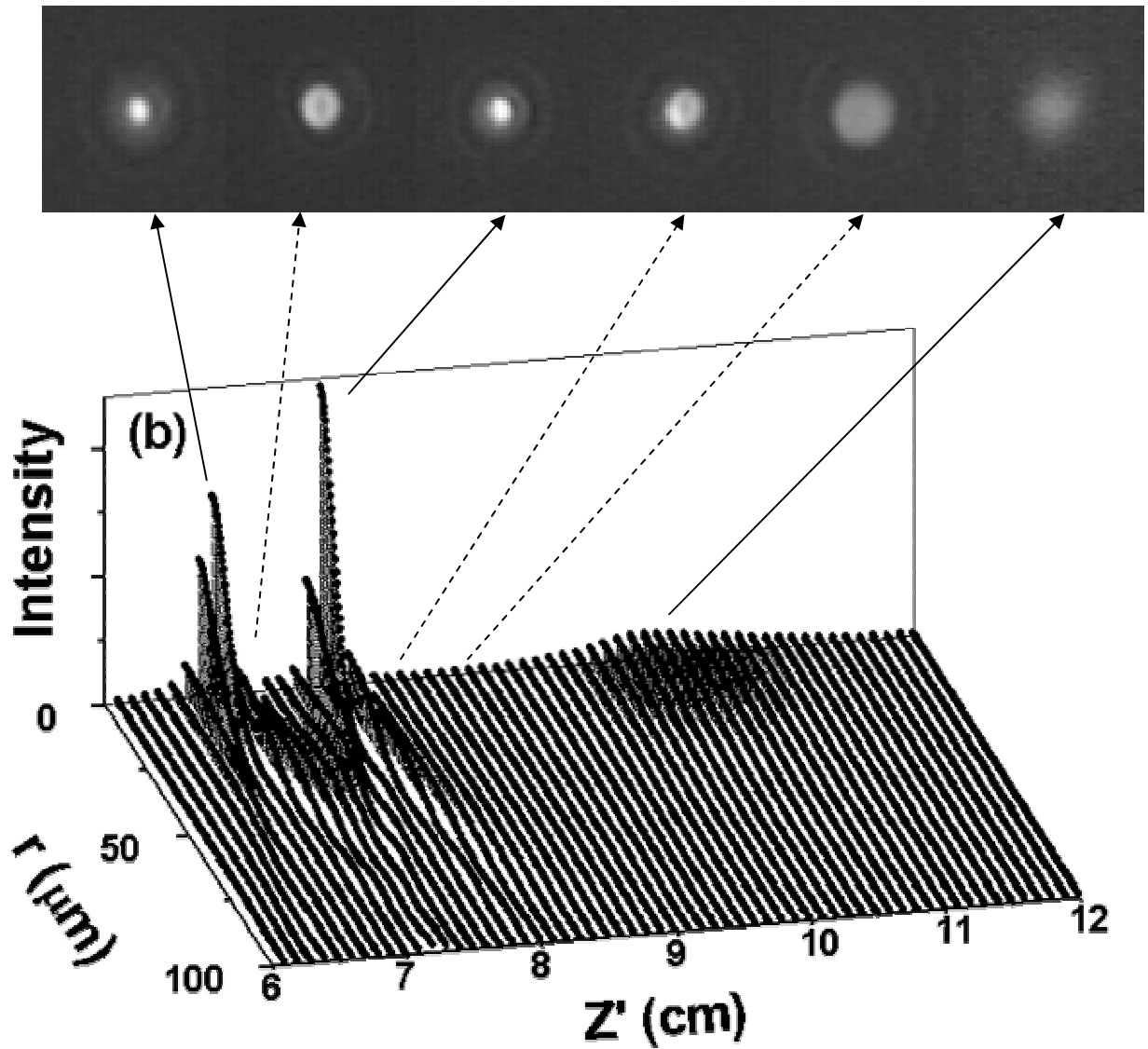
Fig. 3.3. (b) Propagating behavior for L = 6 cm in Fig. 3.2(a) through a transform

lens. The experimental photographs were arranged in their corresponding positions.

Note the correspondence between (a) and (b).
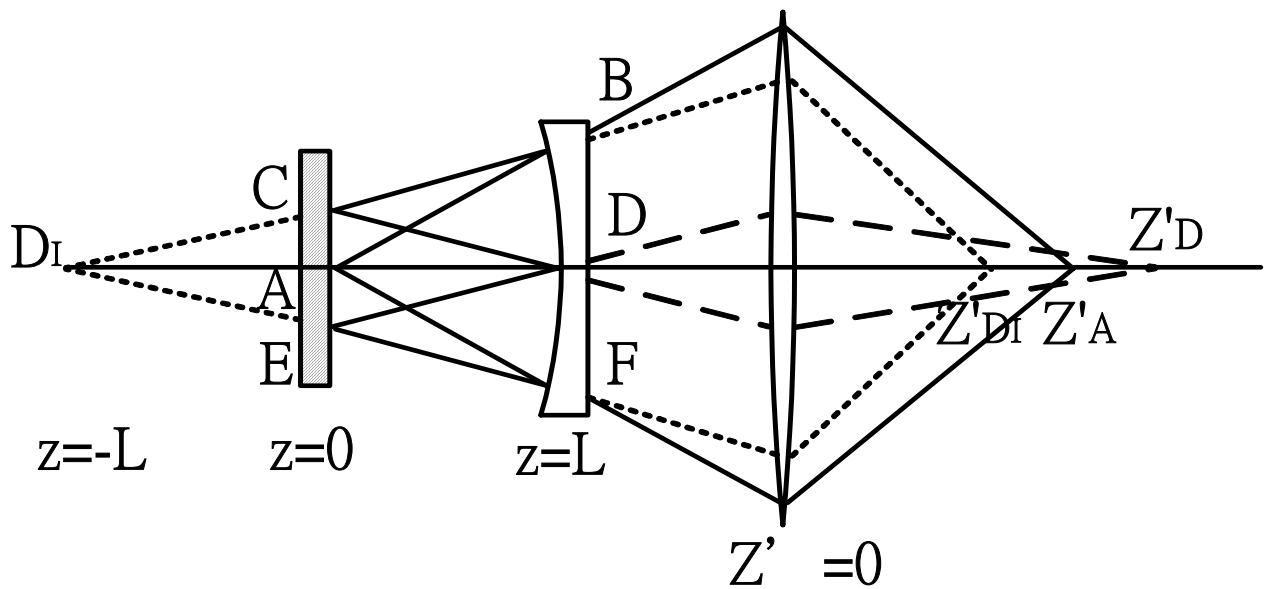
Fig. 3.4. (a) The ray picture for illuminating three sources of the three beam waists for $g_1g_2 = 1/4$. Each round-trip ray emanating from the flat mirror toward the output coupler passes through a focus behind the convergent lens.

(b)

(c)
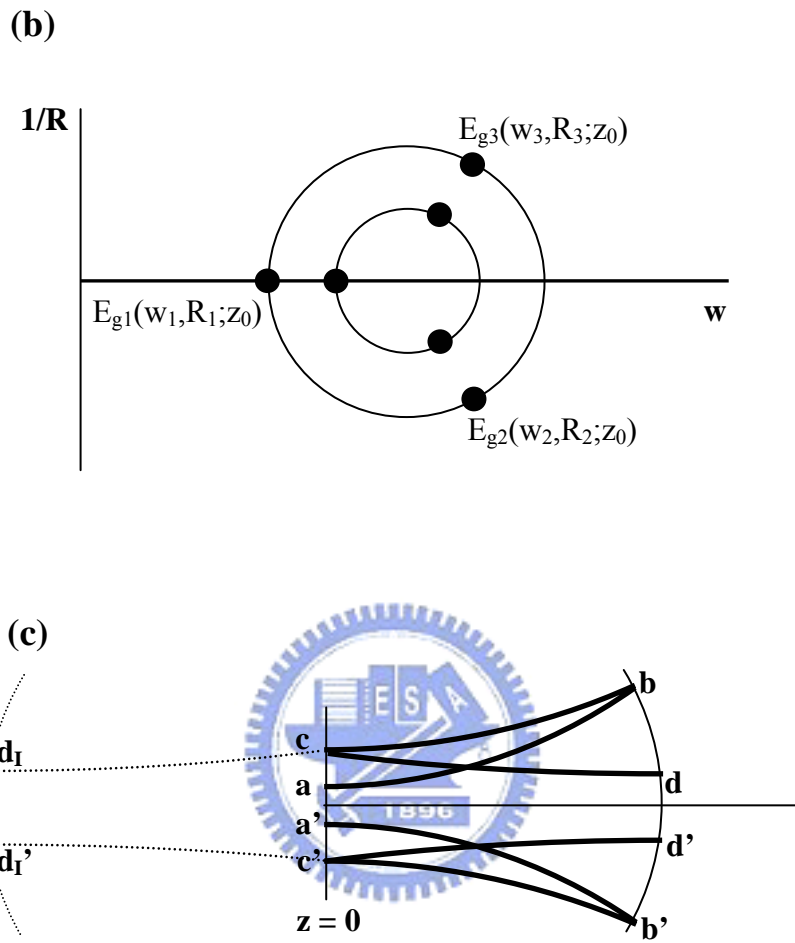
Fig. 3.4. (b) Periodic orbits of q-parameter for the empty cavity. Two circles means there are infinite sets of period-N solutions. (c) The Gaussian beam evolution in the empty cavity.
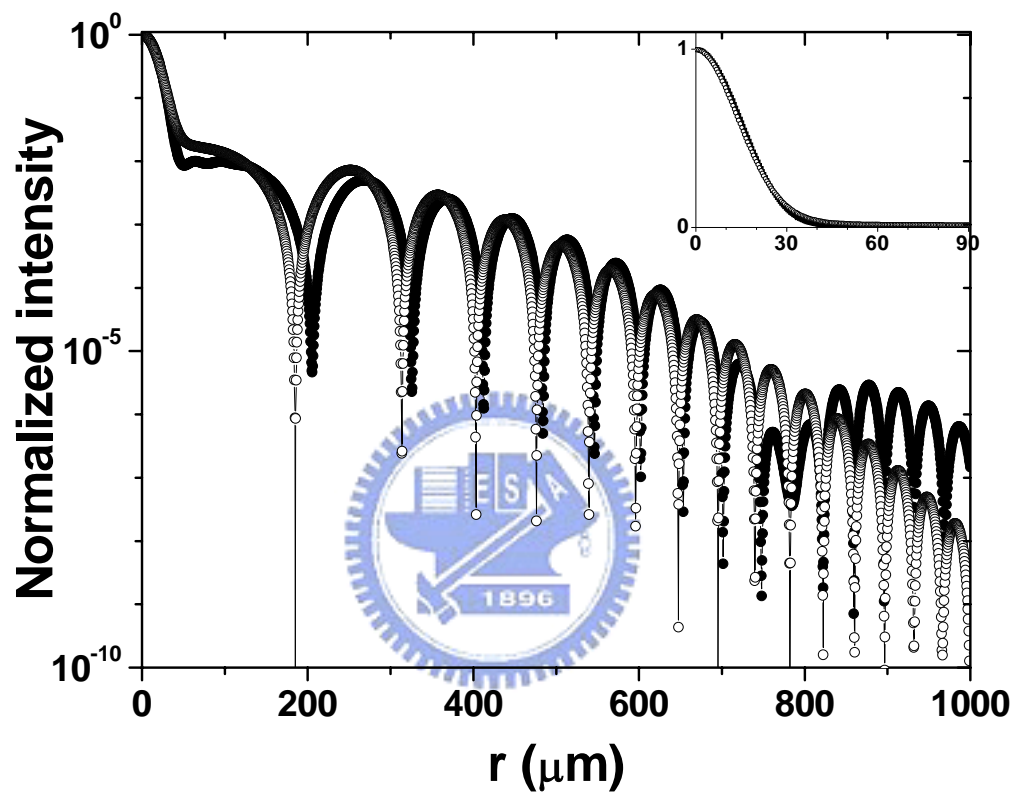
Fig. 3.5.   The normalized intensity profiles of the period-3 superposition mode (open circles) and the self-consistent mode from the mode-calculation (solid circles).   Inset is their central parts with linear scale in the vertical axis.
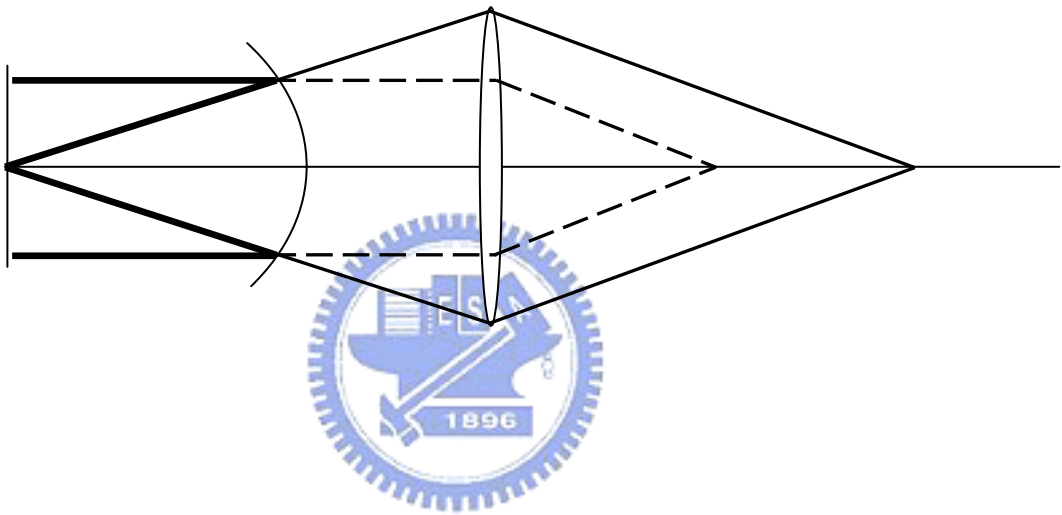
Fig. 3.6. The ray picture for illuminating the two beam waists for $g_1 g_2 = 1/4$. Each round-trip ray emanating from the flat mirror toward the output coupler passes through a focus behind the convergent lens.
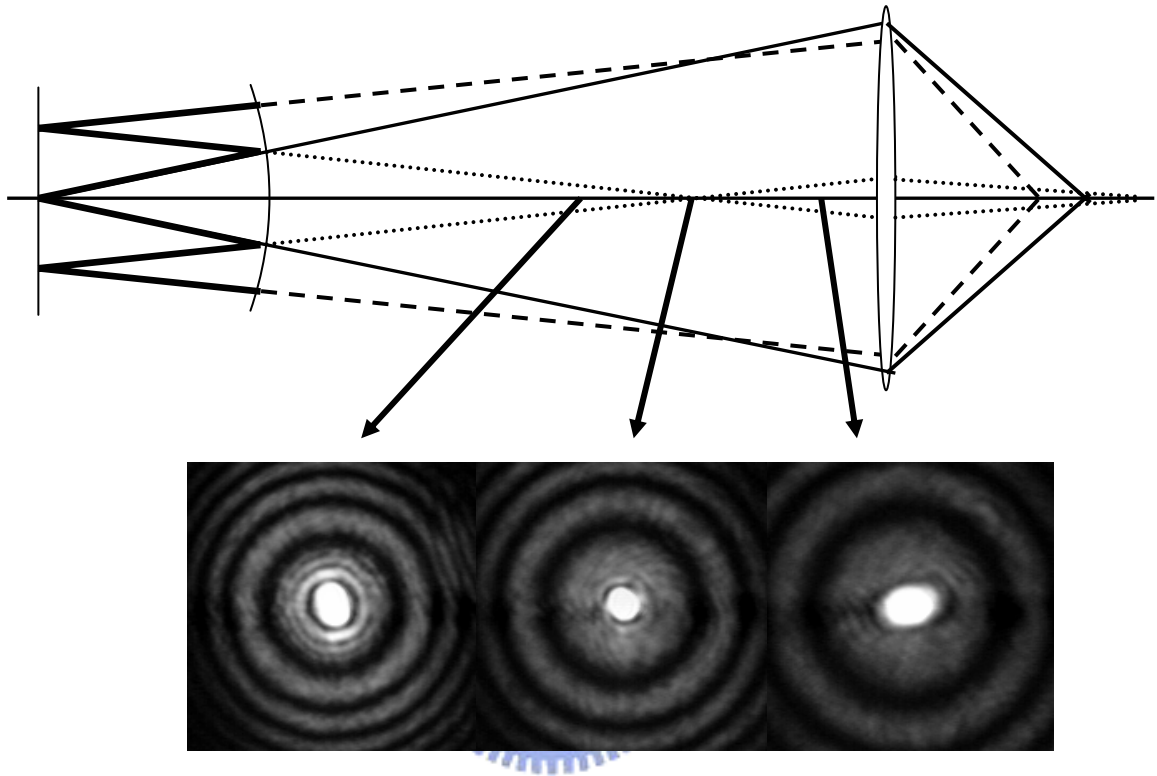
Fig. 3.7. The ray picture similar to Fig. 3.4(a) for $g_1 g_2 = 3/4$ together with three photographs before, at, and after the additional beam waist without passing through the transform lens. The elliptic central parts are due to the astigmatism of the attenuator.
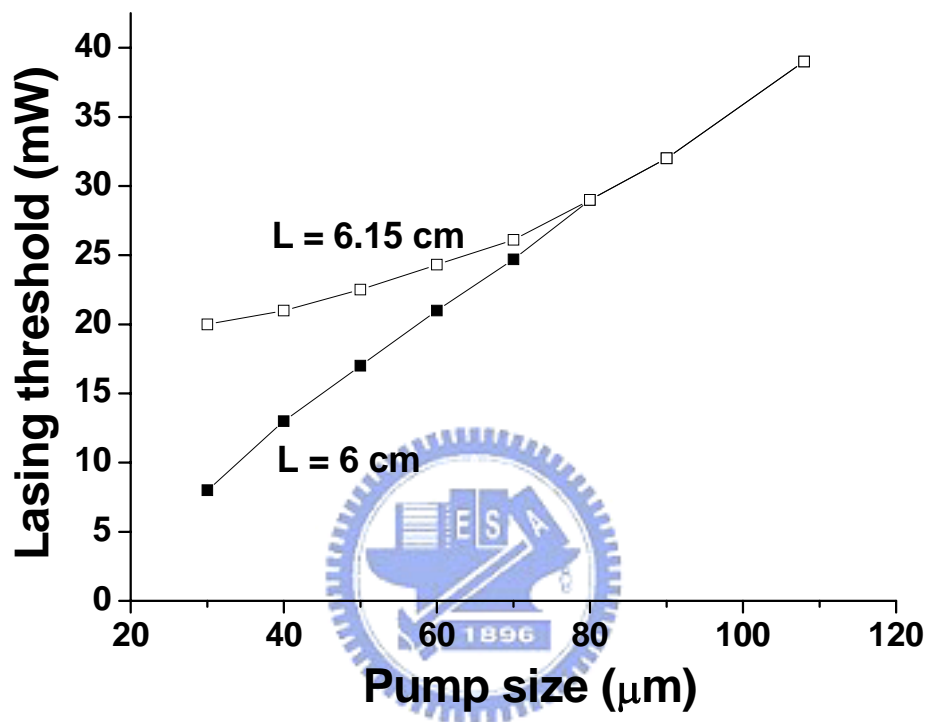
Fig. 3.8. Lasing threshold versus w_p for L = 6 and 6.15 cm.